Photoacoustics 21 (2021) 100221

Contents lists available at ScienceDirect

Photoacoustics

journal homepage: www.elsevier.com/locate/pacs

Clear cell renal cell carcinoma detection by multimodal photoacoustic tomography

Lin Li [a], Hanbo Wu [a], Shuai Hu [b], Yanfei Yu [b], Zhicong Chen [b], Pu Wang [a,c], Liqun Zhou [b], Rui Li [c,3,*], Lin Yao [b,2,*], Shuhua Yue [a,1,*]

[a] Institute of Medical Photonics, Beijing Advanced Innovation Center for Biomedical Engineering, School of Biological Science and Medical Engineering, Beihang University, Beijing 100083, China
[b] Department of Urology, Peking University First Hospital, Beijing 100034, China
[c] Vibronix Inc., West Lafayette, IN, USA

ARTICLE INFO

Keywords:
Photoacoustic tomography
Clear cell renal cell carcinoma
Lipid accumulation

ABSTRACT

There is a need for accurate and rapid detection of renal cancer in clinic. Here, we integrated photoacoustic tomography (PAT) with ultrasound imaging in a single system, which achieved tissue imaging depth about 3 mm and imaging speed about 3.5 cm^2/min. We used the wavelength at 1197 nm to map lipid distribution in normal renal tissues and clear cell renal cell carcinoma (ccRCC) tissues collected from 19 patients undergone nephrectomy. Our results indicated that the photoacoustic signal from lipids was significantly higher in ccRCC tissues than that in normal tissues. Moreover, based on the quantification of lipid area ratio, we were able to differentiate normal and ccRCC with 100 % sensitivity, 80 % specificity, and area under receiver operating characteristic curve of 0.95. Our findings demonstrate that multimodal PAT can differentiate normal and ccRCC by integrating the morphologic information from ultrasound and lipid amount information from vibrational PAT.

1. Introduction

Among the current methods for renal cancer treatment, surgical resection (radical nephrectomy or partial nephrectomy) is still the most effective way [1,2]. Partial nephrectomy can maximize the preservation of kidney function while ensuring the therapeutic effect. However, there is an increased risk of local cancer recurrence and a lower survival rate for having cancer residues left inside the kidney during partial nephrectomy [3,4]. The gold standard of tumor assessment for partial nephrectomy is postoperative histopathology examination. However, its turnaround time is 3–5 days.

Currently, there have been several existing or emerging techniques for intraoperative renal cancer diagnosis. Frozen section analysis has been applied in clinic, and it usually takes 20−30 min. However, the accuracy of frozen section analysis is argued because of the limited sampling of the excised tumor tissue [5–7]. Intraoperative ultrasound imaging has been used for the detection of renal masses, but it lacks chemical selectivity to identify the pathological lesions [8–10]. Structured light illumination microscopy was shown to image the edge of the renal parenchyma at a high speed, but it required the use of fluorescent contrast agent and had very limited imaging depth [11]. Raman spectroscopy and fluorescence diffuse reflectance spectroscopy were used to classify tumor and normal tissues, but could only focus on a few spots of interest [12,13]. More recently, some new techniques have been developed for intraoperative histological diagnosis, such as stimulated Raman scattering microscopy [14], microtomy-assisted photoacoustic microscopy [15], spatial light interference microscopy [16], optical coherence microscopy [17], microscopy with ultraviolet surface excitation [18], but these technologies are limited by either slow imaging speed or small field-of-view. Taken together, these current techniques for renal cancer detection are either limited to low sensitivity (<90 %) or long procedure time to image the entire resected tissue surface with deep tissue penetration. Considering that nephrectomy requires temporary artery block-off no longer than 30 min., a label-free imaging technique for renal cancer diagnosis with high sensitivity and fast speed is desirable.

* Corresponding authors.
E-mail addresses: ruili@vibronixinc.com (R. Li), poparies@163.com (L. Yao), yue_shuhua@buaa.edu.cn (S. Yue).
[1] * Corresponding author:
[2] * Co-corresponding author
[3] * Co-corresponding author

https://doi.org/10.1016/j.pacs.2020.100221
Received 16 February 2020; Received in revised form 22 September 2020; Accepted 3 November 2020
Available online 10 November 2020

Recently, photoacoustic tomography (PAT) has been emerging as an unique noninvasive biomedical imaging tool with strong molecular selectivity and deep tissue penetration [19–22]. In particular, melanoma can be detected based on photoacoustic signals from melanin [23,24]; Prostate cancer [25], ovarian cancer [26], colorectal cancer [27], skin cancer [28] and breast cancer [29,30], can be detected based on photoacoustic signals from blood. As for vibrational PAT, a series of previous work has demonstrated that neutral lipids in biological tissues produce a strong photoacoustic signal at around 1200 nm due to the 2nd overtone absorption of CH stretching vibrations [31–34]. Specifically, the photoacoustic signal from adipose tissues is about 7 times higher than that from blood at around 1200 nm [31]. Based on vibrational PAT of neutral lipid accumulation, breast cancer can be identified, because normal breast tissues contain significantly higher amount of neutral lipids than breast cancer tissues [35,36]. Interestingly, an early study has reported that clear cell renal cell carcinoma (ccRCC), which is the most common and aggressive form of renal cancer [37], contains significantly more neutral lipids in the form of cholesteryl ester than normal renal tissues [38]. Thus, it is promising of using PAT for ccRCC detection based on lipid accumulation.

Herein, we developed a multimodal PAT system that could provide both ultrasound images and 1197 nm wavelength PAT images. PAT images at 1197 nm specifically showed lipid accumulation in 32 intact human tissues collected from 19 patients undergone nephrectomy. Due to the big difference in lipid accumulation between normal and ccRCC tissues, we have achieved a 100 % sensitivity and 80 % specificity for ccRCC detection. This result demonstrated the capability of multimodal PAT to distinguish ccRCC tissues from normal tissues.

2. Materials and methods

2.1. Multimodal PAT system

Our multimodal PAT system was developed based on a customized ultrasound system with 128-channel data acquisition board and a customized all-solid-state Raman laser, which generated 10 Hz pulses with wavelengths at 1197 nm (Fig. 1a). The Raman laser was built based on stimulated Raman scattering process in a gain medium. The output wavelength of Raman laser was determined by the pump wavelength and Raman shift of the medium. With 1064 nm laser light as pump, a Ba $(NO_3)_2$ crystal was used to produce a laser output at 1197 nm. The technical details about the Raman laser can be found in Ref [36]. The performance of the Raman laser, including laser pulse duration, pulse energy stability and laser output power at 1197 nm, was shown in Fig. A.1. The 128-element ultrasound transducer array sends and receives acoustic wave at 18.5 MHz center frequency and a bandwidth of 14 MHz–22 MHz (L22−14vX, Verasonics Inc.).The laser and ultrasound system were connected to a computer for synchronizing time trigger. The excitation laser beam was focused by a convex lens and then coupled into a multimode fiber bundle, which transmitted the light to the sample. As shown in Fig. 1b, Two 45-degree transparent glass slides were placed inside the probe holder to reflect the acoustic waves, making the light and the acoustic wave collinear for better adaptment to the unevenness of the tissue surface. The imaging probe was mounted on a 2D stage for X–Z scanning. The ultrasonic and PAT signals were detected by a 128-element ultrasound transducer array, and then were transmitted to the ultrasound system for post-processing and image reconstruction. To characterize the imaging depth, polyethylene tubes with 1.27 mm outer diameter were imaged in a 2.5 % agarose gel phantom. The SNR of polyethylene tubes was calculated from 20log10 ratio of the mean of PA signal to the standard deviation of the background noise.

2.2. Tissue imaging and processing

This study was approved by an institutional review board. Frozen specimens of human renal tissues were obtained from the tissue bank of Department of Urology in Peking University First Hospital. Before imaging, frozen tissues were first fixed with 4% paraformaldehyde, and then embedded in 2.5 % agarose gel. During imaging, embedded tissues were placed in a bath containing phosphate buffered saline solution, and the front end of the probe was immersed into the solution. The 1197 nm laser with energy density of 82 mJ/cm^2 were utilized for PAT signal excitation, which were below the American National Standards Institute (ANSI) safety standard (100 mJ/cm^2 for nanosecond laser at 1197 nm) [32].

As shown in Fig. 1b, a series of two-dimensional ultrasound and PAT images in X–Y direction were acquired for each tissue by moving the

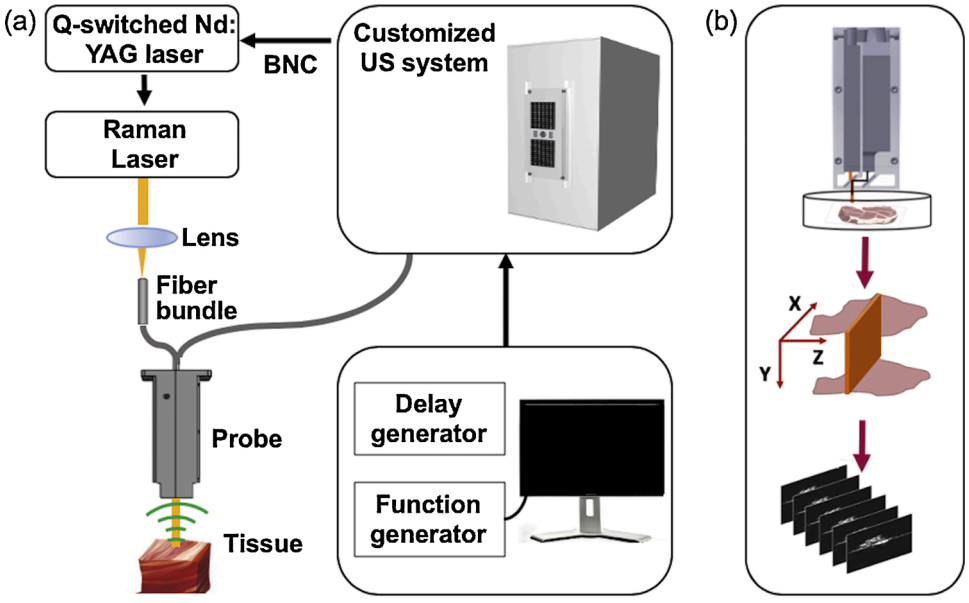

Fig. 1. Schematic of the multimodal PAT system and the procedures of imaging. (a) The PAT system generates the laser output at 1197 nm. The collinear probe combines the optical fiber and the ultrasonic transducer to transmit and receive signals, which are processed by a high-frequency ultrasound imaging system. (b) Schematic to show acquisition of multimodal PAT images. US: ultrasound; PAT: photoacoustic tomography.

probe at a step size of 150 μm. Then, three-dimensional ultrasound and PAT images were reconstructed by ImageJ (NIH, USA), And a single image section from the tissue surface in the X–Z direction was selected for comparison with the histopathology image of the adjacent tissue slice.

2.3. Histopathology

Tissues were peeled from the agarose gel after imaging and dehydrated with a gradient of 30 % sucrose solution overnight at 4 degrees. Then, the tissues were sectioned along the X–Z direction and stained with hematoxylin and eosin (H&E). Finally, two professional pathologists examined the H&E slides independently. According to Fuhrman grading system, renal cancers are given a grade from 1 to 4. Grade 1 and 2 are considered low-grade, and Grade 3 and 4 are considered high-grade.

2.4. Data quantification and statistical analysis

The lipid amount was represented by area ratios between the corresponding areas covered by PAT signals and ultrasound signals. First, we defined the threshold to pick valid signal. The threshold is three times of the noise level, which is estimated as the standard deviation of the background. Then, we calculated the number of pixels from signal to represent the signal area. We defined the area of the PAT signal at 1197 nm as A1 (1197 nm), and the area of the ultrasound signal as A2. Finally, the lipid area ratio was calculated by using the formula 100* *A1 (1197 nm)/A2*. The calculation of the signal area was done by using ImageJ. To compare the lipid amount between different groups, two-sample, Welch's *t*-test was used. $p < 0.05$ was considered statistically significant. The exact *p* values are shown in the corresponding figure captions. To illustrate the ability of using the lipid area ratio to differentiate normal and ccRCC, a receiver operating characteristic (ROC) curve was generated by plotting sensitivity versus (1-specificity) and the area under curve (AUC) was calculated.

3. Results

3.1. Characterization of multimodal PAT system

Our multimodal PAT system, which integrated ultrasound and PAT, was established based on a customized ultrasound system with 128-channel data acquisition and a customized all-solid-state Raman laser. The imaging depth of the system was first measured. The polyethylene tube, rich in C–H bonds, was used to characterize PAT imaging depth at 1197 nm excitation. As shown in Fig. 2**a-b**, both of the upper and lower walls of the polyethylene tubes at different depths can be clearly visualized by ultrasound and PAT. The PAT imaging depth could reach up to 1 cm. The abundant absorption of laser light by the upper wall of the polyethylene tube resulted in the loss of laser energy, and so less laser energy transmitted to the lower wall of the tube. This further led to weaker signals from the lower wall of the tube and showed a thinner tube wall at the bottom. Signal to noise ratio of the PAT signals were then measured at different depths. As shown in Fig. 2c, the signal-to-noise ratio was around 38 dB at 2 mm depth and gradually decreased to 28 dB around 9 mm depth, presumably because the laser power reduced with depth. The spatial resolution was further characterized by imaging a 50 μm diameter tungsten wire placed at ~1 mm beneath the ultrasound transducer. Based on the PAT image of the tungsten wire (Fig. 2d), the lateral and axial resolution was 372 μm and 230 μm, respectively, as shown in Fig. 2**e-f**.

Before multimodal PAT imaging of human renal tissues, we used a beef tissue to test the imaging capabilities. As shown in **Fig. A.2**, by using laser excitation at 1197 nm, we were able to detect strong signals from lipid deposition with ~3 mm depth and reconstruct 3D multimodal PAT image, which was consistent with the photograph of the beef tissue. Moreover, with 12.8 mm * 40 mm field of view and 450 μm/second scanning speed along the z-direction at 150 μm translational step size, the system could assess ~3.5 cm^2 tissue area per minute.

3.2. Multimodal PAT of normal and ccRCC tissues

In order to demonstrate the capability of multimodal PAT system for

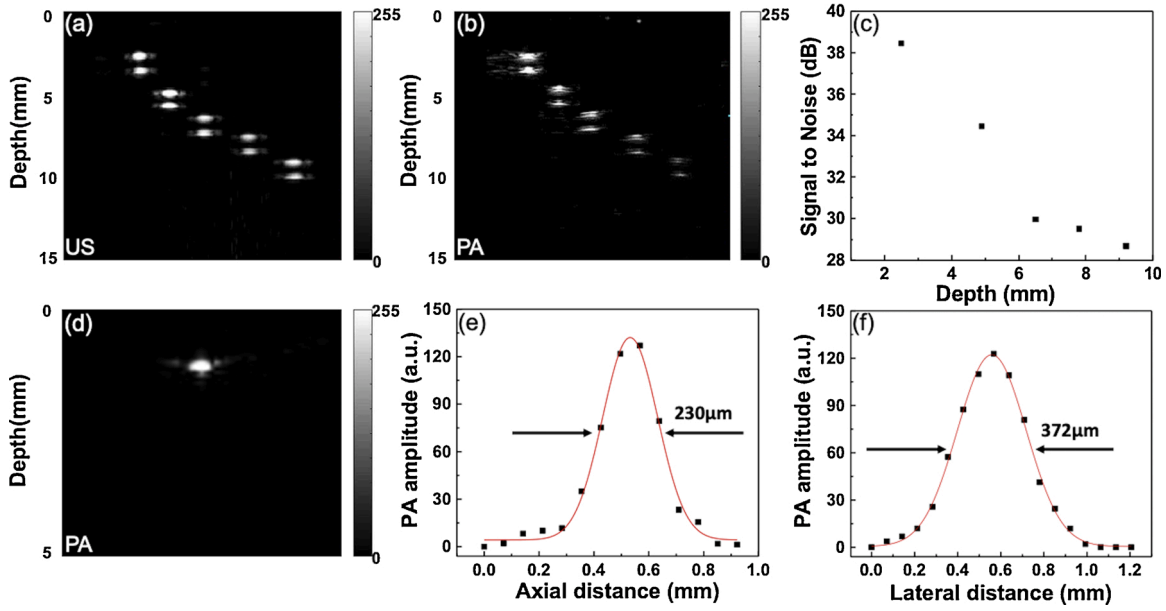

Fig. 2. Characterization of multimodal PAT system performance. (a-b) Ultrasound and PAT images of five polyethylene tubes in an agarose gel phantom at different depths. The PAT images of polyethylene tubes were taken by excitation at 1197 nm. (c) Signal-to-noise ratios of PAT images of polyethylene tubes at different depths. (d) PAT image of a 50 μm tungsten ~1 mm beneath the probe in water. (e) Axial resolution measured at 1 mm depth. (f) Lateral resolution measured at 1 mm depth. The color bar shows the PA amplitude and the unit for the color bar is arbitrary unit. Black spot: experimental data; Red curve: Gaussian fitting curve; US: ultrasound; PAT: photoacoustic tomography.

ccRCC detection, we compared the multimodal PAT images with the histological images at the same location. In total, 32 human renal tissues (15 normal, 12 low-grade ccRCC, 4 high-grade ccRCC and 1 sample containing both cancer and normal tissue) from 19 patients were imaged. The patients information was listed in **Table A.1**. The PAT image at 1197 nm showed the distribution of lipids. Diagnosis was confirmed by histopathology. As shown in Fig. 3, we found abundant lipid signals in the ccRCC tissue, but very little or no detectable lipid signals in the normal tissue. This finding was consistent throughout most of the patient tissues. An enlarged histopathological image of the ccRCC is shown in **Fig. A.3**. More representative images are shown in **Fig. A.4**. Moreover, we assessed the tissue from patient #19, which contained both normal and ccRCC tissue, and found that the lipid signal in the ccRCC area was higher than that in the normal area, consistent with previous results. This demonstrated that multimodal PAT system was able to differentiate normal and ccRCC on the same tissue sample (**Fig. A.5**).

3.3. Differentiation between normal and ccRCC by multimodal PAT

The lipid amount was quantified by the area ratios between the corresponding areas covered by PAT signals and those covered by ultrasound signals. The lipid area ratio was found to be significantly higher (~9 times) in ccRCC tissues than that in normal tissues (Fig. 4a). Although the lipid area ratio was higher in high-grade ccRCC compared to low-grade ccRCC, there was no statistical difference (**Fig. A.6**). Detailed information about lipid area ratios are listed in Table 1 **and Table A.2**.

To test the ability of using the lipid area ratio to differentiate ccRCC from normal tissues, the ROC curve was generated by plotting sensitivity versus (1-specificity), as shown in Fig. 4**b**. The large area under curve (AUC = 0.95) demonstrated that the lipid area ratio can accurately differentiate between normal and ccRCC tissues. Moreover, the ROC curve provided a way to obtain the desired degree of sensitivity at the cost of specificity. Because detection sensitivity is more important for ccRCC detection, the threshold of lipid area ratio was chosen to be 7.62 % to achieve 100 % sensitivity and 80 % specificity.

4. Discussion

There is a need for accurate and rapid detection of renal cancer in clinic. In this work, we developed a customized multimodal PAT system at 1197 nm to detect lipid distribution respectively, at an imaging speed of 3.5 cm^2 tissue area per minute. Our data from 32 intact human tissues demonstrated that the PAT signal of lipids was significantly higher in ccRCC tissues than that in normal tissues. By collecting the morphologic information from ultrasound imaging and lipid area ratio information from vibrational PAT, multimodal PAT can identify ccRCC from normal renal tissues with 100 % sensitivity, 80 % specificity, and the AUC of 0.95. As discussed below, these results demonstrated the potential of using multimodal PAT system for intraoperative ccRCC detection.

First, lipid accumulation can serve as a marker for ccRCC detection. Our data has shown significantly stronger vibrational photoacoustic signals from neutral lipids in ccRCC compared to the normal counterparts, although there is indeed a variation of lipid signal level among different patients. As for the ccRCC tissues with small amount of lipid accumulation, photoacoustic microscopy could help accurate detection owing to high spatial resolution [39–43].

Second, high sensitivity makes our multimodal PAT system a promising way for sensitive ccRCC detection. Tumor residue in partial nephrectomy increases the risk of local cancer recurrence and results in a lower survival rate [3,4].Therefore, it is essential to get high sensitivity of renal cancer detection. In this study, based on the morphological information provided by ultrasound imaging and the lipid amount information provided by PAT imaging, we were able to differentiate normal and ccRCC tissues with 100 % sensitivity and 80 % specificity. Such high sensitivity could help surgeons to remove ccRCC, the most common and aggressive form of renal cancer, as much as possible and leave a healthy kidney.

Third, high speed of our multimodal PAT system fulfills the requirement for intraoperative cancer detection. Since renal tumor masses smaller than 4 cm in diameter can be usually treated by partial nephrectomy, the maximal surface area of the resected renal tumor tissue is about 50 cm^2. With an imaging speed at 3.5 cm^2/min of our system, the whole surface area of the resected tissue can be assessed within 15 min. Such high imaging speed meets the current clinical need

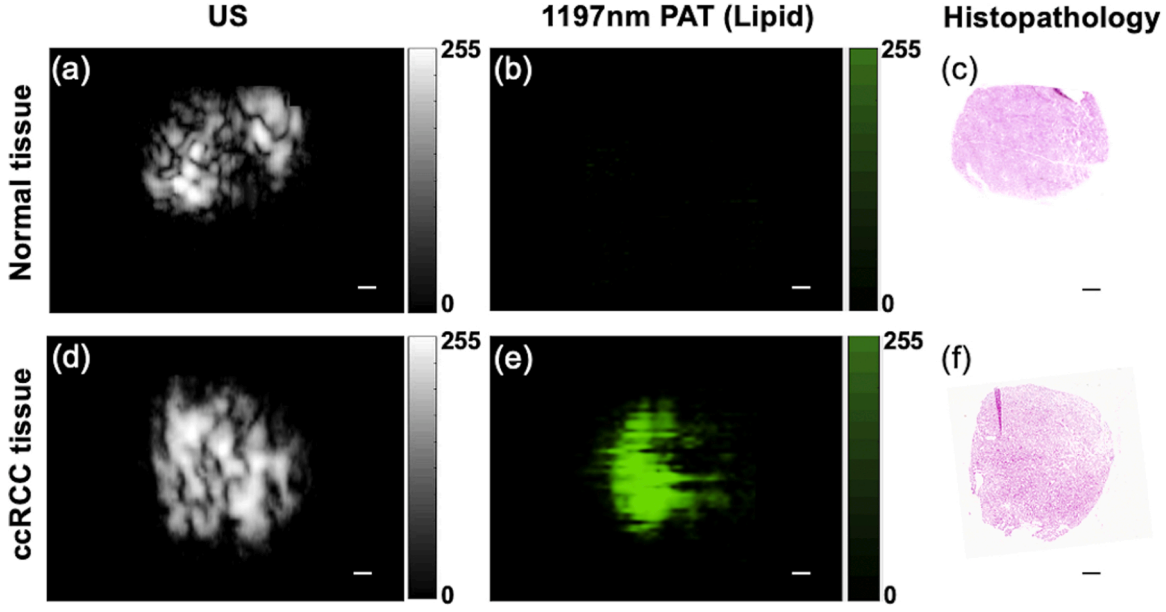

Fig. 3. Representative multimodal PAT images of normal and ccRCC tissues. (a-b) Multimodal PAT images of the normal tissue. (c) H&E image of the corresponding normal tissue. (d-e) Multimodal PAT images of the ccRCC tissue. (f) H&E image of the corresponding ccRCC tissue. Grey color: US image; Green color: PAT image at 1197 nm; Scalar bars, 1 mm. ccRCC: clear cell renal cell carcinoma; The color bar shows the PA amplitude and the unit for the color bar is arbitrary unit. US: ultrasound; PAT: photoacoustic tomography.

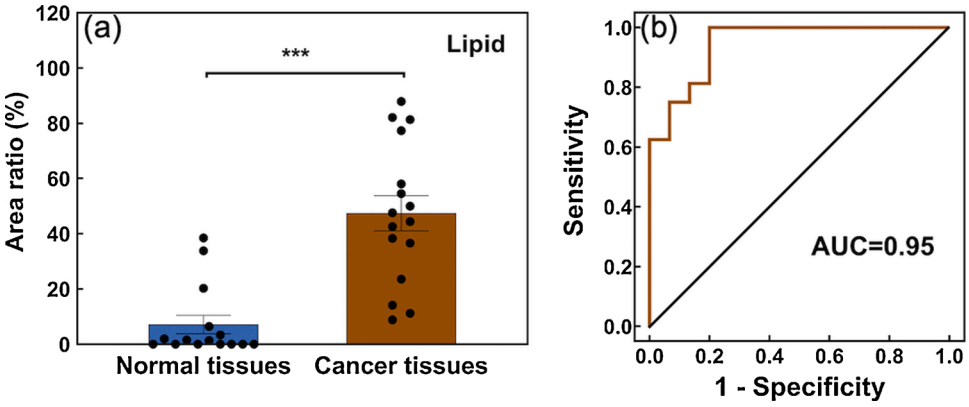

Fig. 4. Differentiation between normal and ccRCC tissues by multimodal PAT system. (a) The lipid area ratios in normal and ccRCC tissues, respectively. The scattered dots represent area ratios for each tissue. Error bars represent the standard error of the mean (SEM). *** $p < 0.0001$; n.s., not significant. (b) The ROC curve illustrating the ability of using the lipid area ratio to distinguish normal tissues and ccRCC tissues (orange curve). The closer the curve comes to the 45-degree diagonal (black line), the less accurate the diagnostic test. ROC: receiver operating characteristic; ccRCC: clear cell renal cell carcinoma; AUC: area under curve.

Table 1
Lipid area ratios in normal and ccRCC tissues.

	n[a]	Lipid area ratio (%) (mean ± SEM[c])
Normal	15	7.15 ± 3.33
ccRCC[b]	16	47.40 ± 6.38
Low-grade ccRCC	12	44.22 ± 6.60
High-grade ccRCC	4	56.93 ± 17.19

[a]N represents the number of tissues;
[b]Clear cell renal cell carcinoma;
[c]Standard error of the mean.
* The results of each sample keep two decimals.

for rapid intraoperative renal cancer detection.

Finally, we utilized a customized Raman laser as the excitation light source, which showed greater efficiency to generate 1197 nm laser light output for photoacoustic imaging of lipids, compared with traditional optical parametric oscillator. Due to its excellent performance, the Raman laser-based photoacoustic imaging has been reported in many previous work [36,46,47]. Owing to the compact size and cost-effective feature, the Raman laser shows great promise for clinical translation.

5. Conclusions

In this study, we developed a multimodal PAT system with 1197 nm excitation to map both lipid distribution in intact human renal tissues collected from nephrectomy. Our data indicated that the PAT signal from lipids was significantly higher in ccRCC tissues than that in normal tissues. Based on the lipid amount information obtained from PAT and the morphological information provided by ultrasound imaging, we were able to differentiate normal and ccRCC tissues with 100 % sensitivity and 80 % specificity. Our results show promise of using multimodal PAT system for intraoperative ccRCC detection.

Transparency document

The Transparency document associated with this article can be found in the online version.

Declaration of Competing Interest

The authors declare that there are no conflicts of interest.

Acknowledgments

This work was supported by the Fundamental Research Funds for the Central Universities [grant number YWF-19-BJ-J-214]; the "Excellent Hundred Talents" Program start-up fund from Beihang University. We greatly appreciate the technical support from Vibronic Inc. for imaging system development.

Appendix A. Supplementary data

Supplementary material related to this article can be found, in the online version, at doi:https://doi.org/10.1016/j.pacs.2020.100221.

References

[1] A. Becker, L. Pradel, L. Kluth, M. Schmid, C. Eichelberg, S. Ahyai, Q. Trinh, D. Seiler, R. Dahlem, J. Hansen, Laparoscopic versus open partial nephrectomy for clinical T1 renal masses: no impact of surgical approach on perioperative complications and long-term postoperative quality of life, World J. Urol. 33 (2015) 421–426, https://doi.org/10.1007/s00345-014-1318-1.
[2] J.S. Pak, J.J. Lee, K. Bilal, M. Finkelstein, M.A. Palese, Utilization trends and outcomes up to 3 months of open, laparoscopic, and robotic partial nephrectomy, J. Robot. Surg. 11 (2017) 223–229, https://doi.org/10.1007/s11701-016-0650-4.
[3] E.O. Kwon, B.S. Carver, M.E. Snyder, P. Russo, Impact of positive surgical margins in patients undergoing partial nephrectomy for renal cortical tumours, BJU Int. 99 (2007) 286–289, https://doi.org/10.1111/j.1464-410X.2006.06623.x.
[4] K. Bensalah, A.J. Pantuck, N. Rioux-Leclercq, R. Thuret, F. Montorsi, P. I. Karakiewicz, N. Mottet, L. Zini, R. Bertini, L. Salomon, A. Villers, M. Soulie, L. Bellec, P. Rischmann, A. De La Taille, R. Avakian, M. Crepel, J.M. Ferriere, J. C. Bernhard, T. Dujardin, F. Pouliot, J. Rigaud, C. Pfister, B. Albouy, L. Guy, S. Joniau, H. van Poppel, T. Lebret, T. Culty, F. Saint, A. Zisman, O. Raz, H. Lang, R. Spie, A. Wille, J. Roigas, A. Aguilera, B. Rambeaud, L.M. Piñeiro, O. Nativ, R. Farfara, F. Richard, M. Roupret, C. Doehn, P.J. Bastian, S.C. Muller, J. Tostain, A.S. Belldegrun, J.J. Patard, Positive surgical margin appears to have negligible impact on survival of renal cell carcinomas treated by nephron-sparing surgery, Eur. Urol. 57 (2010) 466–471, https://doi.org/10.1016/j.eururo.2009.03.048.
[5] A. Breda, S.V. Stepanian, J. Liao, J.S. Lam, G. Guazzoni, M. Stifelman, K. Perry, A. Celia, G. Breda, P. Fornara, S. Jackman, A. Rosales, J. Palou, M. Grasso, V. Pansadoro, V. Disanto, F. Porpiglia, C. Milani, C. Abbou, R. Gaston, G. Janetschek, N.A. Soomro, J. de la Rosette, M.P. Laguna, P.G. Schulam, Positive margins in laparoscopic partial nephrectomy in 855 cases: a multi-institutional survey from the United States and Europe, J. Urol. 178 (2007) 47–50, https://doi.org/10.1016/j.juro.2007.03.045.
[6] H. Van Poppel, S. Joniau, How important are surgical margins in nephron-sparing surgery? Eur. Urol. Suppl. 6 (2007) 533–539, https://doi.org/10.1016/j.eursup.2007.01.007.
[7] D.J. Kubinski, P.E. Clark, D.G. Assimos, M.C. Hall, Utility of frozen section analysis of resection margins during partial nephrectomy, Urology 64 (2004) 31–34, https://doi.org/10.1016/j.urology.2004.03.011.
[8] F.M. Alharbi, C.K. Chahwan, S.G. Le Gal, K.M. Guleryuz, X.P. Tillou, A.P. Doerfler, Intraoperative ultrasound control of surgical margins during partial nephrectomy, Urol. Ann. 8 (2016) 430–433, https://doi.org/10.4103/0974-7796.192107.
[9] A. Doerfler, A. Oitchayomi, X. Tillou, A simple method for ensuring resection margins during laparoscopic partial nephrectomy: the intracorporeal ultrasonography, Urology. 84 (2014) 1240–1242, https://doi.org/10.1016/j.urology.2014.07.025.
[10] B. Qin, H. Hu, Y. Lu, Y. Wang, Y. Yu, J. Zhang, Z. Zhang, H. Gao, Q. Wang, S. Wang, Intraoperative ultrasonography in laparoscopic partial nephrectomy for intrarenal tumors, PLoS One 13 (2018) e0195911, https://doi.org/10.1371/journal.pone.0195911.
[11] M. Wang, D.B. Tulman, A.B. Sholl, S.H. Mandava, M.M. Maddox, B.R. Lee, J. Quincy Brown, Partial nephrectomy margin imaging using structured illumination microscopy, J. Biophotonics 11 (2018), https://doi.org/10.1002/jbio.201600328 e201600328.
[12] K. Bensalah, J. Fleureau, D. Rolland, O. Lavastre, N. Rioux-Leclercq, F. Guillé, J. J. Patard, L. Senhadji, R. De Crevoisier, Raman spectroscopy: a novel experimental

approach to evaluating renal tumours, Eur. Urol. 58 (2010) 602–608, https://doi.org/10.1016/j.eururo.2010.06.002.
[13] D.J. Parekh, W.C. Lin, S.D. Herrell, Optical spectroscopy characteristics can differentiate benign and malignant renal tissues: a potentially useful modality, J. Urol. 174 (2005) 1754–1758, https://doi.org/10.1097/01.ju.0000177484.33596.c9.
[14] T.C. Hollon, B. Pandian, A.R. Adapa, E. Urias, A.V. Save, S.S.S. Khalsa, D. G. Eichberg, R.S. D'Amico, Z.U. Farooq, S. Lewis, Near real-time intraoperative brain tumor diagnosis using stimulated Raman histology and deep neural networks, Nat. Med. 26 (2020) 52–58, https://doi.org/10.1038/s41591-019-0715-9.
[15] T.T.W. Wong, R. Zhang, C. Zhang, H.C. Hsu, K.I. Maslov, L. Wang, J. Shi, R. Chen, K.K. Shung, Q. Zhou, L.V. Wang, Label-free automated three-dimensional imaging of whole organs by microtomy-assisted photoacoustic microscopy, Nat. Commun. 8 (2017) 1–8, https://doi.org/10.1038/s41467-017-01649-3.
[16] H. Majeed, T.H. Nguyen, M.E. Kandel, A. Kajdacsy-Balla, G. Popescu, Label-free quantitative evaluation of breast tissue using Spatial Light Interference Microscopy (SLIM), Sci. Rep. 8 (2018) 1–9, https://doi.org/10.1038/s41598-018-25261-7.
[17] Y. Ma, T. Xu, X. Huang, X. Wang, C. Li, J. Jerwick, Y. Ning, X. Zeng, B. Wang, Y. Wang, Z. Zhang, X. Zhang, C. Zhou, Computer-aided diagnosis of label-free 3-D optical coherence microscopy images of human cervical tissue, IEEE Trans. Biomed. Eng. 66 (2018) 2447–2456, https://doi.org/10.1109/TBME.2018.2890167.
[18] F. Fereidouni, Z.T. Harmany, M. Tian, A. Todd, J.A. Kintner, J.D. McPherson, A. D. Borowsky, J. Bishop, M. Lechpammer, S.G. Demos, R. Levenson, Microscopy with ultraviolet surface excitation for rapid slide-free histology, Nat. Biomed. Eng. 1 (2017) 957–966, https://doi.org/10.1038/s41551-017-0165-y.
[19] L.V. Wang, J. Yao, A practical guide to photoacoustic tomography in the life sciences, Nat. Methods 13 (2016) 627–638, https://doi.org/10.1038/nmeth.3925.
[20] L.V. Wang, S. Hu, Photoacoustic tomography: in vivo imaging from organelles to organs, Science. 335 (2012) 1458–1462, https://doi.org/10.1126/science.1216210.
[21] J. Jo, C. Tian, G. Xu, J. Sarazin, E. Schiopu, G. Gandikota, X. Wang, Photoacoustic tomography for human musculoskeletal imaging and inflammatory arthritis detection, Photoacoustics. 12 (2018) 82–89, https://doi.org/10.1016/j.pacs.2018.07.004.
[22] T. Vu, D. Razansky, J. Yao, Listening to tissues with new light: recent technological advances in photoacoustic imaging, J. Opt. 21 (2019) 103001, https://doi.org/10.1088/2040-8986/ab3b1a.
[23] P. Hai, Y. Zhou, R. Zhang, J. Ma, Y. Li, J.Y. Shao, L.V. Wang, Label-free high-throughput detection and quantification of circulating melanoma tumor cell clusters by linear-array-based photoacoustic tomography, J. Biomed. Opt. 22 (2016), 041004, https://doi.org/10.1117/1.jbo.22.4.041004.
[24] J. Jose, D.J. Grootendorst, T.W. Vijn, M.W. Wouters, H. van Boven, T.G. van Leeuwen, W. Steenbergen, T.J.M. Ruers, S. Manohar, Initial results of imaging melanoma metastasis in resected human lymph nodes using photoacoustic computed tomography, J. Biomed. Opt. 16 (2011), 096021, https://doi.org/10.1117/1.3631705.
[25] B.L. Bungart, L. Lan, P. Wang, R. Li, M.O. Koch, L. Cheng, T.A. Masterson, M. Dundar, J.X. Cheng, Photoacoustic tomography of intact human prostates and vascular texture analysis identify prostate cancer biopsy targets, Photoacoustics. 11 (2018) 46–55, https://doi.org/10.1016/j.pacs.2018.07.006.
[26] A. Aguirre, Y. Ardeshirpour, M.M. Sanders, M. Brewer, Q. Zhu, Potential role of coregistered photoacoustic and ultrasound imaging in ovarian cancer detection and characterization, Transl. Oncol. 4 (2011) 29–37, https://doi.org/10.1593/tlo.10187.
[27] W.C. Chapman, M. Mutch, Co-registered photoacoustic and ultrasound imaging of human colorectal cancer, J. Biomed. Opt. 24 (2019) 1850008, https://doi.org/10.1117/1.jbo.24.12.121913.
[28] Z. Chen, E. Rank, K.M. Meiburger, C. Sinz, A. Hodul, E. Zhang, E. Hoover, M. Minneman, J. Ensher, P.C. Beard, H. Kittler, R.A. Leitgeb, W. Drexler, M. Liu, Non-invasive multimodal optical coherence and photoacoustic tomography for human skin imaging, Sci. Rep. 7 (2017) 17975, https://doi.org/10.1038/s41598-017-18331-9.
[29] S.A. Ermilov, T. Khamapirad, A. Conjusteau, M.H. Leonard, R. Lacewell, K. Mehta, T. Miller, A.A. Oraevsky, Laser optoacoustic imaging system for detection of breast cancer, J. Biomed. Opt. 14 (2009) 24007, https://doi.org/10.1117/1.3086616.
[30] L. Lin, P. Hu, J. Shi, C.M. Appleton, K. Maslov, L. Li, R. Zhang, L.V. Wang, Single-breath-hold photoacoustic computed tomography of the breast, Nat. Commun. 9 (2018) 1–9, https://doi.org/10.1038/s41467-018-04576-z.
[31] H.W. Wang, N. Chai, P. Wang, S. Hu, W. Dou, D. Umulis, L.V. Wang, M. Sturek, R. Lucht, J.X. Cheng, Label-free bond-selective imaging by listening to vibrationally excited molecules, Phys. Rev. Lett. 106 (2011) 238106, https://doi.org/10.1103/PhysRevLett.106.238106.
[32] M. Xu, L.V. Wang, Photoacoustic imaging in biomedicine, Rev. Sci. Instrum. 77 (2006), 041101, https://doi.org/10.1063/1.2195024.
[33] K. Jansen, A.F. van der Steen, M. Wu, H.M. van Beusekom, G. Springeling, X. Li, Q. Zhou, K. Kirk Shung, D.P. de Kleijn, G. van Soest, Spectroscopic intravascular photoacoustic imaging of lipids in atherosclerosis, J. Biomed. Opt. 19 (2014), 026006, https://doi.org/10.1117/1.jbo.19.2.026006.
[34] K. Jansen, M. Wu, A.F.W. van der Steen, G. van Soest, Lipid detection in atherosclerotic human coronaries by spectroscopic intravascular photoacoustic imaging, Opt. Express 21 (2013) 21472–21484, https://doi.org/10.1364/oe.21.021472.
[35] R. Li, P. Wang, L. Lan, F.P. Lloyd Jr., C.J. Goergen, S. Chen, J.X. Cheng, Assessing breast tumor margin by multispectral photoacoustic tomography, Biomed. Opt. Express 6 (2015) 1273–1281, https://doi.org/10.1364/BOE.6.001273.
[36] R. Li, L. Lan, Y. Xia, P. Wang, L.K. Han, G.L. Dunnington, S. Obeng-Gyasi, G. E. Sandusky, J.A. Medley, S.T. Crook, J.X. Cheng, High-speed intra-operative assessment of breast tumour margins by multimodal ultrasound and photoacoustic tomography, Med. Devices Sens. 1 (2018) e10018, https://doi.org/10.1002/mds3.10018.
[37] V.F. Muglia, A. Prando, Renal cell carcinoma: histological classification and correlation with imaging findings, Radiol. Bras. 48 (2015) 166–174, https://doi.org/10.1590/0100-3984.2013.1927.
[38] R.L. Gebhard, R.V. Clayman, W.F. Prigge, R. Figenshau, N.A. Staley, C. Reesey, A. Bear, Abnormal cholesterol metabolism in renal clear cell carcinoma, J. Lipid Res. 28 (1987) 1177–1184.
[39] S. Hu, L.V. Wang, Optical-resolution photoacoustic microscopy: auscultation of biological systems at the cellular level, Biophys. J. 105 (2013) 841–847, https://doi.org/10.1016/j.bpj.2013.07.017.
[40] S. Hu, K. Maslov, V. Tsytsarev, L.V. Wang, Functional transcranial brain imaging by optical-resolution photoacoustic microscopy, J. Biomed. Opt. 14 (2009), 040503, https://doi.org/10.1117/1.3194136.
[41] L. Lin, J. Yao, R. Zhang, C.C. Chen, C.H. Huang, Y. Li, L. Wang, W. Chapman, J. Zou, L.V. Wang, High-speed photoacoustic microscopy of mouse cortical microhemodynamics, J. Biophotonics 10 (2017) 792–798, https://doi.org/10.1002/jbio.201600236.
[42] W. Liu, D.M. Shcherbakova, N. Kurupassery, Y. Li, Q. Zhou, V.V. Verkhusha, J. Yao, Quad-mode functional and molecular photoacoustic microscopy, Sci. Rep. 8 (2018) 1–10, https://doi.org/10.1038/s41598-018-29249-1.
[43] Q. Chen, H. Guo, T. Jin, W. Qi, H. Xie, L. Xi, Ultracompact high-resolution photoacoustic microscopy, Opt. Lett. 43 (2018) 1615–1618, https://doi.org/10.1364/OL.43.001615.
[46] B.C. Wilkinson, T.C. Sheehan, T. Buma, Spectroscopic photoacoustic microscopy in the 1064-1300 nm range using a pulsed multi-color source based on stimulated Raman scattering, IEEE Int, Ultrason. Symp. IUS, IEEE Computer Society (2014) 25–28.
[47] H.M. Pask, S. Myers, J.A. Piper, J. Richards, T. McKay, High average power, all-solid-state external resonator Raman laser, Opt. Lett. 28 (2003) 435, https://doi.org/10.1364/ol.28.000435.

Lin Li is currently a graduate student in School of Biological Science and Medical Engineering at Beihang University. She received her bachelor degree from Xidian University in 2017 and joined Prof. Shuhua Yue's lab, focusing on the application of photoacoustic tomography for renal cancer diagnosis.

Hanbo Wu is a visiting student in School of Biological Science and Medical Engineering at Beihang University.

Shuai Hu is a pathologist at the Department of Urology, Peking University First Hospital. He completed his M.D. at the Peking University in 2014. Her research mainly focuses on the urology pathology.

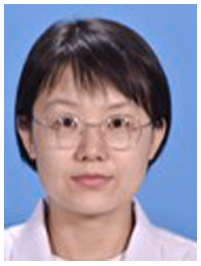

Yanfei Yu is a pathologist at the Department of Urology, Peking University First Hospital. She graduated from Peking University School of Medicine in 2019 with a master degree. Her research mainly focuses on the urology pathology.

Zhicong Chen graduated from the Department of Clinical Medicine in Shantou University. He is currently a PhD student in the Peking University First Hospital. His research focuses on urinary system tumor metastasis and tumor metabolism.

Pu Wang is a professor of the School of Biological Science and Medical Engineering at Beihang University in China. He received his Ph.D. in 2014 from Weldon School of Biomedical engineering at Purdue University with expertise in multimodal microscopy and photoacoustic imaging.

Liqun Zhou is currently the director of Peking University Department of Urology. He graduated from Bethune Medical University with a bachelor degree in 1987. He graduated from Beijing Medical University in 1992 with a doctorate degree in medicine. He has been engaged in clinical and scientific research in urology. His professional expertise is urogenital tumors and endoscopic urological surgery. The scientific research work mainly focuses on the molecular etiology of urogenital tumors.

Rui Li works for Vibronix Inc. He received his PhD degree in 2017 from Weldon School of Biomedical Engineering at Purdue University with expertise in photoacoustic imaging.

Lin Yao is currently the urologist at Peking University First Hospital. He graduated from the Peking University School of Medicine as M.D. His professional expertise is in the diagnosis and treatment of urological tumors, including prostate cancer, renal cancer, bladder cancer, etc.

Shuhua Yue is now an Associate Professor of School of Biological Science and Medical Engineering at Beihang University in China. She got her bachelor degree in Tsinghua University and her Ph.D. degree from Purdue University in the US. Her research focuses on the study of cancer cell metabolism by label-free spectroscopic imaging and development of novel cancer diagnosis methods.